Computational single-photon depth imaging without transverse regularization

COMPUTATIONAL SINGLE-PHOTON DEPTH IMAGING WITHOUT TRANSVERSE REGULARIZATION

Dongeek Shin[1] *Jeffrey H. Shapiro*[1] *Vivek K Goyal*[2]

[1]Massachusetts Institute of Technology, Cambridge, MA 02139
[2]Boston University, Boston, MA 02215

ABSTRACT

Depth profile reconstruction of a scene at low light levels using an active imaging setup has wide-ranging applications in remote sensing. In such low-light imaging scenarios, single-photon detectors are employed to time-resolve individual photon detections. However, even with single-photon detectors, current frameworks are limited to using hundreds of photon detections at each pixel to mitigate Poisson noise inherent in light detection. In this paper, we discuss two pixelwise imaging frameworks that allow accurate reconstruction of depth profiles using small numbers of photon detections. The first framework addresses the problem of depth reconstruction of an opaque target, in which it is assumed that each pixel contains exactly one reflector. The second framework addresses the problem of reconstructing multiple-depth pixels. In each scenario, our framework achieves photon efficiency by combining accurate statistics for individual photon detections with a longitudinal sparsity constraint tailored to the imaging problem. We demonstrate the photon efficiencies of our frameworks by comparing them with conventional imagers that use more naïve models based on high light-level assumptions.

Index Terms— Single-photon imaging, depth imaging, convex optimization, greedy algorithm, LIDAR, Poisson processes

1. INTRODUCTION

The technique of light detection and ranging (LIDAR), which typically uses a pulsed, narrow-beam light source and a photodetector, reconstructs scene depth by measuring the time-of-flight (ToF) of the backreflected return from each pixel [1]. If there are multiple reflections from the scene, such as when imaging through a scattering medium, then multiple times-of-flight are recorded for multi-depth reconstruction [2]. By transverse-scanning the light source and repeating the pixelwise ToF acquisition process, one can obtain a spatially-resolved depth profile of a scene.

Many LIDAR systems have employed single-photon detectors [3–5]. Because the single-photon detector is able to resolve individual photon detections, it can be useful for low-light applications such as remote 3D sensing, in which light travels long distances and only a small amount of flux is incident at the detector. However, even when using single-photon detectors, the acquisition times of the system are made long enough to detect hundreds of photons per pixel, such that a finely binned histogram of detection times approximates the continuous-time, continuous-amplitude incident flux with appropriate normalization, making ToF estimation straightforward.

This material is based upon work supported in part by a Samsung Scholarship, the U.S. National Science Foundation under Grant No. 1422034, and the MIT Lincoln Laboratory Advanced Concepts Committee.

Very recently, computational imaging frameworks have been introduced to process photon detection data without treating a detection-time histogram as approximating a flux waveform, and using regularization predicated on piecewise smoothness in the transverse dimensions [6–10]. For natural scenes, accurate results have been demonstrated from as little as 1 detected photon per pixel, even in the presence of significant ambient light. However, in some applications, it is important to avoid regularization based on piecewise smoothness. For example, when spatial features are small relative to the pixel spacing, methods dependent on such regularization often produce erroneously over-smoothed results.

In this paper, we present a pixelwise imaging framework from [11, Ch. 1–3], [12, 13] for accurate depth-profile reconstruction using only a small number of photon detections in the presence of ambient background light. This framework achieves high photon efficiency using an accurate Poisson process model of photon detections and longitudinal sparsity constraints, based on discreteness of scene reflectors, but no transverse regularization. We concentrate on modeling, algorithms, and simulations for two imaging scenarios.

Imaging single-reflector depth: For imaging the depth of a single reflector per pixel, our framework uses the accurate Poisson observation model for photon detections plus a union-of-subspaces constraint that models reflector sparsity and the unknown background flux. By using a greedy signal reconstruction algorithm—a novel variation on compressive sampling matching pursuit (CoSaMP) [14]—we solve for accurate estimates of scene depth and background flux in a pixelwise manner. Using simulations of single-photon LIDAR, we demonstrate that our proposed imaging framework outperforms log-matched filtering, which is the conventional maximum-likelihood (ML) depth estimator in the absence of background flux [15]. Experimental results are presented in [12].

Imaging multiple depths: For imaging multiple reflectors per pixel, with the number of reflectors unknown, our framework uses the accurate Poisson observation model for photon detections plus a sparsity constraint on the multi-depth profile signal. In this problem, we assume background flux is calibrated and known. We show that the multi-depth estimation problem from photon detections can be relaxed to create a convex optimization problem, and we solve it using a novel variation on the iterative shrinkage-thresholding algorithm (ISTA) [16]. Using simulations of single-photon LIDAR, we demonstrate that our proposed imaging framework outperforms the Gaussian-mixture fitting method, which is the conventional multi-depth estimator assuming a large number of photon detections [17]. Experimental results are presented in [13].

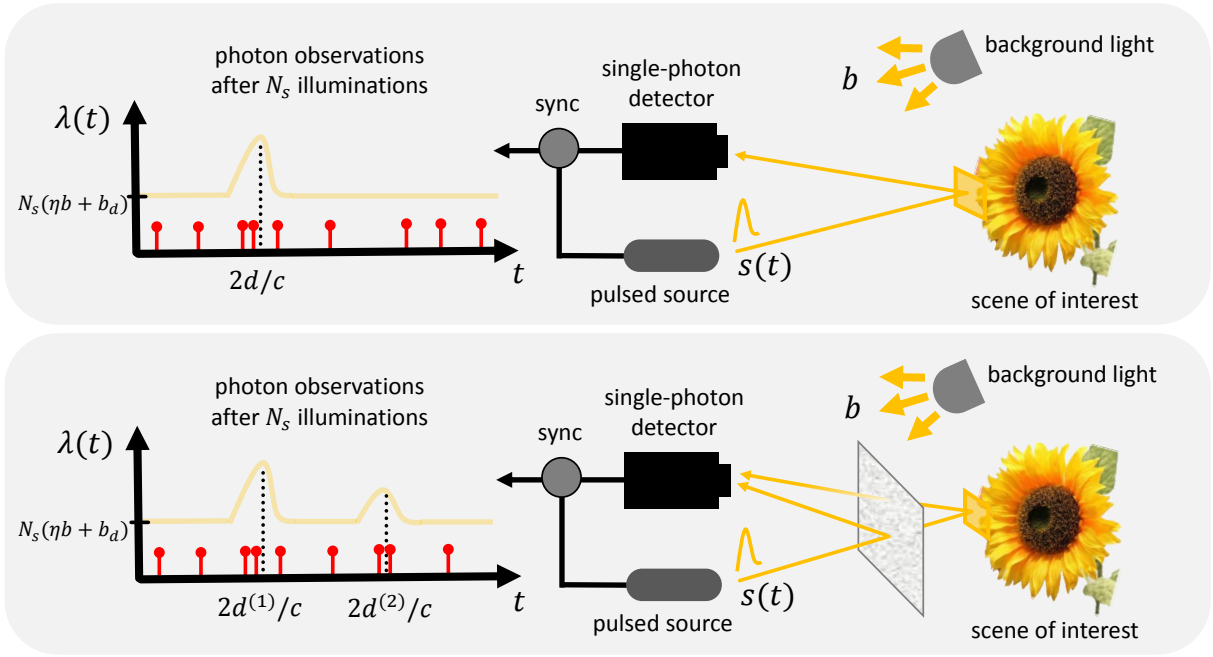

Fig. 1. Imaging setup with a raster-scanning pulsed source and a single-pixel single-photon detector for (top) single-reflector depth reconstruction and (bottom) multi-depth reconstruction (two-reflector case). The aim in both imaging scenarios is to use the discrete photon time-stamps (shown in red markers) to reconstruct the scene depth (or the set of depths) at a pixel.

2. SINGLE-PHOTON DEPTH IMAGING SETUP

Figure 1 illustrates our single-photon LIDAR setup for the two imaging scenarios. In both scenarios, a focused optical source, such as a laser, illuminates a pixel in the scene with the pulse waveform $s(t)$ that starts at time 0 and has root mean-square pulsewidth T_p. This illumination is repeated every T_r seconds for a sequence of N_s pulses. The single-photon detector, in conjunction with a time correlator, is used to time stamp individual photon detections relative to the time at which the immediately preceding pulse was transmitted. The plots at the left of the two setup figures show the raw photon detection dataset after N_s trials of illumination and detection. These detection times are observations of a time-inhomogeneous Poisson process whose rate function combines contributions from pixel return, background light, and dark counts. They are used to estimate the depth profile for the illuminated pixel. In the single-reflector imaging setup (top figure), the aim is to estimate a single scene depth and, in the multi-reflector imaging setup (bottom figure), the aim is to reconstruct multiple scene depths.

3. PHOTON DETECTION MODEL

We first derive the relationship between the pixelwise impulse response, which contains information about reflector depths, and the photon-detection times. Our derivation is for a single pixel; the same model applies at each pixel.

Let $r(t)$ for $t \in [0, T_r)$ be the optical flux, in photons per second, that is incident on the detector from a single pulse illumination. Then, we can write

$$r(t) = (h*s)(t)+b, \tag{1}$$

where $h(t)$ is the impulse response of the scene pixel, b is the constant background-light flux, and $*$ denotes convolution. The rate function $\lambda(t)$ that characterizes the photon detections at the single-photon detector is thus

$$\lambda(t) = \eta(h_d*r)(t)+b_d, \tag{2}$$

where $\eta \in (0, 1)$, b_d, and $h_d(t)$ are the detector's efficiency, dark-count rate, and response function, respectively. For simplicity, we assume a normalized detector response function: $\int_0^{T_r} h_d(t)\, dt = 1$. Substituting (1) into (2) then gives

$$\lambda(t) = \eta(h*\tilde{s})(t)+(\eta b+b_d), \tag{3}$$

where $\tilde{s} = h_d*s$ is the effective pulse waveform after accounting for the detector response. We assume that the scene being imaged is entirely within the maximum unambiguous range of the imager, so $h(t) = 0$ for $t > T_r$. We also assume $T_p \ll T_r$ so that $(h*\tilde{s})(t) = 0$ for $t \notin [0, T_r)$. Furthermore, the effect of detector dead time (reset time) is omitted. The skewing of the effective pulse waveform due to dead time that arises from moderate- to high-flux conditions is described in [11, App. B].

A time-correlated single-photon detector records the time-of-detection of a photon within a timing resolution of Δ seconds. We can choose a pulse repetition period that is much longer than the timing resolution ($\Delta \ll T_r$) so that $m = \lceil T_r/\Delta \rceil$ is the number of time bins that contain photon detections. Using the probabilistic theory of photon detection [15], the kth bin of the observed photon count histogram after N_s pulse illuminations is easily shown to be distributed as

$$\mathbf{y}_k \sim \text{Poisson}\left(\underbrace{N_s\eta \int_{(k-1)\Delta}^{k\Delta} (h*\tilde{s})(t)\, dt}_{\substack{\text{Mean count of} \\ \text{signal photons}}} + \underbrace{N_s\Delta(\eta b+b_d)}_{\substack{\text{Mean count of} \\ \text{background photons} \\ \text{plus dark counts}}} \right). \tag{4}$$

We would like to reach an approximation in which the Poisson rate parameter of $\mathbf{y}_k$ is expressed as an affine transformation with respect to the scene impulse-response vector. By approximating $(h*\tilde{s})(t)$ with a sampling period of $\Delta' = T_r/n$ for some $n \in \mathbb{Z}^+$, we can write the first term in the Poisson parameter in (4) as

$$\begin{aligned} & N_s\eta \int_{(k-1)\Delta}^{k\Delta} (h*\tilde{s})(t)\,dt \\ &= \int_{(k-1)\Delta}^{k\Delta} \int_0^{T_r} N_s\eta h(y)\tilde{s}(t-y)\,dy\,dt \\ &\overset{(a)}{=} \int_{(k-1)\Delta}^{k\Delta} \sum_{j=1}^{n} \int_{(j-1)\Delta'}^{j\Delta'} N_s\eta h(y)\tilde{s}(t-y)\,dy\,dt \\ &\overset{(b)}{\approx} \sum_{j=1}^{n} \int_{(k-1)\Delta}^{k\Delta} \int_{(j-1)\Delta'}^{j\Delta'} \frac{\mathbf{x}_j}{\Delta'} \frac{\mathbf{S}_{k,j}}{\Delta}\,dy\,dt \;=\; \sum_{j=1}^{n} \mathbf{S}_{k,j}\,\mathbf{x}_j, \end{aligned}$$

where (a) follows from partitioning $[0, T_r)$ into n subintervals and (b) from using constant approximations for $h(y)$ and $N_s\eta\tilde{s}(t-y)$ on $(y,t) \in [(j-1)\Delta', j\Delta') \times [(k-1)\Delta, k\Delta)$; specifically,

$$\mathbf{x}_j = \int_{(j-1)\Delta'}^{j\Delta'} h(y)\,dy,$$

$$\mathbf{S}_{k,j} = \frac{1}{\Delta'} \int_{(k-1)\Delta}^{k\Delta} \int_{(j-1)\Delta'}^{j\Delta'} N_s\eta\tilde{s}(t-y)\,dy\,dt,$$

for $k = 1, 2, \ldots, m,\ j = 1, 2, \ldots, n$. Based on our discrete approximation, the observation model of (4) can be rewritten as

$$\mathbf{y}_k \sim \text{Poisson}\left((\mathbf{S}\mathbf{x} + B\mathbb{1}_m)_k \right), \quad \text{for } k = 1, 2, \ldots, m, \tag{5}$$

where $\mathbf{x}$ is an $n \times 1$ vector, $\mathbf{S}$ is an $m \times n$ matrix, and $\mathbb{1}_m$ is an $m \times 1$ vector of ones, and $B = N_s\Delta(\eta b + b_d)$.

4. NOVEL IMAGING FRAMEWORK

Using the accurate photon detection statistics derived in the previous section, we consider solving the inverse problem of depth profile reconstruction in the two imaging scenarios from Fig. 1.

4.1. Imaging a single depth per pixel

For the single-depth imaging problem, we consider $\mathbf{x}$ and B as unknown variables. Defining $\mathbf{A} = [\mathbf{S}, \mathbb{1}_m]$ and $\mathbf{z} = [\mathbf{x}^T, B]^T$, such that all unknown variables are represented by a single vector $\mathbf{z}$, we can further rewrite (5) as

$$\mathbf{y}_k \sim \text{Poisson}\big((\mathbf{A}\mathbf{z})_k \big). \tag{6}$$

Since $\mathbf{x}$ has exactly one nonzero entry due to our opaque reflector assumption, we have that $\mathbf{z}$ lies in the union of n subspaces defined as

$$\mathsf{UOS}(n) = \bigcup_{k=1}^{n} \left\{ \mathbf{z} \in \mathbb{R}^{n+1} : \mathbf{z}_{\{1,2,\ldots,n\}\setminus\{k\}} = 0 \right\}. \tag{7}$$

Figure 2 shows an illustration of $\mathsf{UOS}(2)$, which is a nonconvex set. Thus, $\hat{\mathbf{z}}$, a statistically accurate estimate of $\mathbf{z}$, can be obtained by solving the constrained likelihood optimization problem:

$$\begin{aligned} \underset{\mathbf{z}}{\text{minimize}} \quad & \mathcal{L}_{\mathbf{z}}(\mathbf{z}; \mathbf{A}, \mathbf{y}) \\ \text{subject to} \quad & \mathbf{z} \in \mathsf{UOS}(n), \\ & \mathbf{z}_i \geq 0, \quad i = 1, 2, \ldots, (n+1), \end{aligned} \tag{8}$$

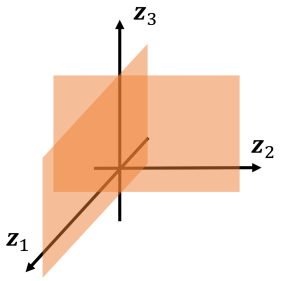

Fig. 2. Illustration of the nonconvex set $\mathsf{UOS}(2)$.

where $\mathcal{L}_{\mathbf{z}}(\mathbf{z}; \mathbf{A}, \mathbf{y})$ is the negative log-likelihood function of $\mathbf{z}$ based on (6). To solve (8), which is an optimization problem over a nonconvex union-of-subspaces set, we use a greedy algorithm inspired by CoSaMP. Unlike CoSaMP, each of whose iterations projects the solution onto the best subspace of the ℓ_0-norm ball, we project our solution onto the best subspace of $\mathcal{S}_n$. (Here the best subspace is defined as the subspace closest to the intermediate solution in terms of Euclidean distance.) The details of the algorithm implementation can be found in [11, Ch. 2], [12].

4.2. Imaging multiple depths per pixel

For the multi-depth imaging problem, we consider the scenario in which the impulse response vector $\mathbf{x}$ is unknown, but B is known through calibration prior to active imaging.

We use the K-reflector model for describing the impulse response of a pixel with multiple reflectors [18, 19]:

$$h(t) = \sum_{i=1}^{K} a^{(i)} \delta\Big(t - 2d^{(i)}/c\Big), \qquad t \in [0, T_r), \tag{9}$$

where $a^{(i)}$ and $d^{(i)}$ are respectively the reflectivity and depth values of the ith reflector at an image pixel, $\delta(\cdot)$ denotes the Dirac delta function, and K is the number of reflectors. If the minimum depth separation of adjacent reflectors is larger than $c\Delta'/2$, then $\mathbf{x}$ has exactly K nonzero entries whose values are $\{a^{(i)}\}_{i=1}^{K}$.

We can minimize the negative log-likelihood function, while including a K-sparsity constaint on $\mathbf{x}$, to solve for the multi-depth profile. However, the K-sparsity constaint, which is expressed using the ℓ_0-norm, makes the problem NP-hard [20]. To design a computationally feasible algorithm, we apply the convex relaxation that uses the ℓ_1-norm as a convex-hull proxy for the ℓ_0-norm [21]. Our optimization program also includes a nonnegativity constraint on reflectivity estimates. Thus, we obtain the multi-depth profile estimate $\hat{\mathbf{x}}$ by solving the following ℓ_1-penalized and constrained likelihood optimization problem:

$$\begin{aligned} \underset{\mathbf{x}}{\text{minimize}} \quad & \mathcal{L}_{\mathbf{x}}(\mathbf{x}; \mathbf{y}, \mathbf{S}, B) + \beta\|\mathbf{x}\|_1 \\ \text{subject to} \quad & \mathbf{x}_k \geq 0, \quad k = 1, 2, \ldots, n, \end{aligned} \tag{10}$$

where $\mathcal{L}_{\mathbf{x}}(\mathbf{x}; \mathbf{y}, \mathbf{S}, B)$ is the negative log-likelihood of $\mathbf{x}$ from (5) and $\beta > 0$ is the parameter controlling the degree of penalizing the estimate's lack of sparsity. Because $\mathcal{L}_{\mathbf{x}}(\mathbf{x}; \mathbf{y}, \mathbf{S}, B)$ and the ℓ_1-norm are both convex functions in $\mathbf{x}$ and the nonnegative constraint is a convex set, the minimization problem given in (10) is a convex optimization problem. Thus, its global optimum can be found by using gradient descent methods. As post-processing, we replace the

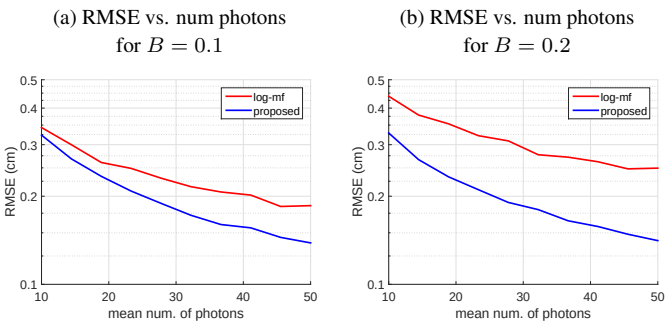

Fig. 3. Simulation of pixelwise depth imaging results from the conventional log-matched filter and our methods, when using photon detections at two background levels.

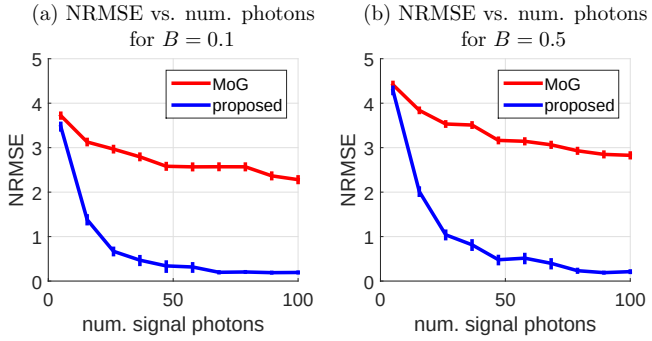

Fig. 4. Simulation of pixelwise two-depth imaging results from the conventional MoG and our methods at two background levels. Signal photon detections are detections from scene response and not the background-light plus dark-count detections. Here NRMSE $= 1$ corresponds to an unnormalized mean-squared error of $cT_p/2 = 4.5$ cm. The plots also include confidence bars for the ± 1 standard errors.

clusters of depths (neighboring nonzero entries of $\hat{\mathbf{x}}$) with their respective average depths to maximize the sparsity level of the signal. The details of the algorithm implementation can be found in [11, Ch. 3], [13].

5. SIMULATION RESULTS

For single-depth imaging, we simulated (6) to study the performance of the proposed framework. We compared our joint depth plus background estimation method with the conventional log-matched filter, which is the ML depth solution assuming $B = 0$:

$$\hat{d}_{\text{ML}} = \frac{c\Delta'}{2}\left(\underset{i\in\{1,2,\ldots,n\}}{\arg\max}\ \log \mathbf{S}_i^T \mathbf{y}\right). \tag{11}$$

Figure 3 shows the root-mean-square error (RMSE) of depth reconstruction at two different background levels. Here we used $m = n = 801$ and a Gaussian pulse with T_p such that $cT_p/2 = 1$ cm. For each number of photon detections, 4000 Monte Carlo trials of (6) were run. We observe that our method improves over conventional log-matched filtering for both background levels, with greater improvements seen in the high background case, due to our modeling of both impulse response and background as unknown variables.

For multi-depth imaging, we studied the performance for $K = 2$, which is used in applications such as second-order multipath interference mitigation [22] and looking through a scattering layer [23] via ToF imaging. We compared two algorithms: the mixture-of-Gaussian (MoG) estimator using greedy histogram fitting, and our proposed imager that uses convex optimization. Let $\{d^{(1)}, d^{(2)}\}$, with $d^{(1)} < d^{(2)}$, be the set of true depths of the two reflectors at a pixel. Also, let $\{\hat{d}^{(1)}, \hat{d}^{(2)}\}$, with $\hat{d}^{(1)} < \hat{d}^{(2)}$, be the set of identified depths obtained using either the MoG method or our proposed framework. We used the pulsewidth-normalized root mean-square error (NRMSE) to study multi-depth recovery performance of the two algorithms:

$$\begin{aligned}&\text{NRMSE}\left(\{d^{(1)}, d^{(2)}\}, \{\hat{d}^{(1)}, \hat{d}^{(2)}\}\right)\\ &= \frac{1}{cT_p/2}\sqrt{\mathbb{E}\left[0.5((d^{(1)}-\hat{d}^{(1)})^2+(d^{(1)}-\hat{d}^{(2)})^2)\right]}.\end{aligned} \tag{12}$$

If NRMSE is below 1, then the imager has achieved sub-pulsewidth depth accuracy. (When either algorithm reported more than two values, the two with the highest amplitudes were used in computing the NRMSE.)

Figure 4 shows simulated performance results of pixelwise two-depth estimation using the MoG-based method and our convex optimization method for two background levels. Here we had $m = n = 100$, $T_p = 0.3$ ns, and $\Delta = 1$ ns. The pulse shape was discrete Gaussian. For each number of photon detections, the number of Monte Carlo trials was 2000. For each Monte Carlo trial, two entries out of n were generated in a uniformly random fashion from n-choose-2 possible combinations to simulate a 2-reflector scene. Also, both entries' amplitudes were set to 1. We used the expectation-maximization (EM) algorithm to perform Gaussian mixture fitting on the photon detection data. For our algorithm, we chose the regularization parameter $\beta = B$, using the assumption that higher penalty for lack of sparsity is required for higher background levels. We see that for both low and high background levels, our proposed framework uniformly outperforms the existing MoG method for various numbers of detected signal photons, i.e., detected photons that had been backreflected from the scene. For example, for both $B = 0.1$ and $B = 0.5$, the difference in RMSE between our framework and MoG is around 9 cm given 10 signal photon detections.

6. CONCLUSIONS

This paper summarizes the imaging framework from [11, Ch. 1–3], [12, 13] for pixelwise reconstruction of single depth and multiple depths per pixel using single-photon ToF data. In both settings, high photon efficiency is achieved using Poisson process photon detection modeling combined with sparsity of discrete-time flux vectors arising from longitudinal sparsity of reflectors. The two settings illustrate both greedy and convex relaxation-based approaches to exploiting sparsity while maintaining computational tractability.

Our pixelwise imaging framework can potentially be useful in low light-level imaging applications, in which the scene is sparsely scanned such that filtering techniques that exploit patchwise smoothness potentially wash out those details. For example, it can be useful in airborne remote sensing [24], whose goal is to recover finely-featured 3D terrain maps from the fewest scans.

7. REFERENCES

[1] B. Schwarz, "LIDAR: mapping the world in 3D," *Nat. Photon.*, vol. 4, no. 7, pp. 429–430, 2010.

[2] C. Mallet and F. Bretar, "Full-waveform topographic lidar: State-of-the-art," *ISPRS J. Photogramm. Remote Sensing*, vol. 64, no. 1, pp. 1–16, 2009.

[3] S. Pellegrini, G. S. Buller, J. M. Smith, A. M. Wallace, and S. Cova, "Laser-based distance measurement using picosecond resolution time-correlated single-photon counting," *Meas. Sci. Techn.*, vol. 11, no. 6, pp. 712, 2000.

[4] B. F. Aull, A. H. Loomis, D. J. Young, R. M. Heinrichs, B. J. Felton, P. J. Daniels, and D. J. Landers, "Geiger-mode avalanche photodiodes for three-dimensional imaging," *Lincoln Lab. J.*, vol. 13, no. 2, pp. 335–349, 2002.

[5] A. McCarthy, R. J. Collins, N. J. Krichel, V. Fernández, A. M. Wallace, and G. S. Buller, "Long-range time-of-flight scanning sensor based on high-speed time-correlated single-photon counting," *Appl. Optics*, vol. 48, no. 32, pp. 6241–6251, 2009.

[6] A. Kirmani, D. Venkatraman, D. Shin, A. Colaço, F. N. C. Wong, J. H. Shapiro, and V. K. Goyal, "First-photon imaging," *Science*, vol. 343, no. 6166, pp. 58–61, 2014.

[7] D. Shin, A. Kirmani, V. K. Goyal, and J. H. Shapiro, "Computational 3D and reflectivity imaging with high photon efficiency," in *Proc. IEEE Int. Conf. Image Process.*, 2014, pp. 46–50.

[8] D. Shin, A. Kirmani, V. K. Goyal, and J. H. Shapiro, "Photon-efficient computational 3-d and reflectivity imaging with single-photon detectors," *IEEE Trans. Comput. Imaging*, vol. 1, no. 2, pp. 112–125, June 2015.

[9] Y. Altmann, X. Ren, A. McCarthy, G. S. Buller, and S. McLaughlin, "Lidar waveform-based analysis of depth images constructed using sparse single-photon data," *IEEE Trans. Image Process.*, vol. 25, no. 5, pp. 1935–1946, May 2016.

[10] D. Shin, F. Xu, D. Venkatraman, R. Lussana, F. Villa, F. Zappa, V. K. Goyal, F. N. C. Wong, and J. H. Shapiro, "Photon-efficient computational imaging with a single-photon camera," in *Proc. Computational Optical Sensing and Imaging, part of OSA Imaging and Applied Optics*, Heidelberg, Germany, July 2016.

[11] D. Shin, *Computational Imaging with Small Numbers of Photons*, Ph.D. thesis, Massachusetts Institute of Technology, Cambridge, MA, Feb. 2016.

[12] D. Shin, J. H. Shapiro, and V. K. Goyal, "Single-photon depth imaging using a union-of-subspaces model," *IEEE Signal Process. Lett.*, vol. 22, no. 12, pp. 2254–2258, Dec. 2015.

[13] D. Shin, F. Xu, F. N. C. Wong, J. H. Shapiro, and V. K. Goyal, "Computational multi-depth single-photon imaging," *Opt. Expr.*, vol. 24, no. 3, pp. 1873–1888, Feb. 2016.

[14] D. Needell and J. A. Tropp, "CoSaMP: Iterative signal recovery from incomplete and inaccurate samples," *Appl. Comput. Harmon. Anal.*, vol. 26, no. 3, pp. 301–321, 2009.

[15] D. L. Snyder, *Random Point Processes*, Wiley, New York, 1975.

[16] I. Daubechies, M. Defrise, and C. De Mol, "An iterative thresholding algorithm for linear inverse problems with a sparsity constraint," *Commun. Pure Appl. Math.*, vol. 57, no. 11, pp. 1413–1457, 2004.

[17] Å. Persson, U. Söderman, J. Töpel, and S. Ahlberg, "Visualization and analysis of full-waveform airborne laser scanner data," in *Proc. ISPRS Workshop Laser Scanning*, 2005, vol. 36, pp. 103–108.

[18] A. M. Wallace, J. Ye, N. J. Krichel, A. McCarthy, R. J. Collins, and G. S. Buller, "Full waveform analysis for long-range 3d imaging laser radar," *EURASIP J. Adv. Signal Process.*, vol. 2010, no. 33, 2010.

[19] D. Freedman, Y. Smolin, E. Krupka, I. Leichter, and M. Schmidt, "SRA: Fast removal of general multipath for TOF sensors," in *Proc. Europ. Conf. Comput. Vis. (ECCV)*, pp. 234–249. Springer, 2014.

[20] B. K. Natarajan, "Sparse approximate solutions to linear systems," *SIAM J. Comput.*, vol. 24, no. 2, pp. 227–234, Apr. 1995.

[21] M. Elad, *Sparse and Redundant Representations: From Theory to Applications in Signal and Image Processing*, Springer Science & Business Media, New York, 2010.

[22] S. Fuchs, M. Suppa, and O. Hellwich, "Compensation for multipath in ToF camera measurements supported by photometric calibration and environment integration," in *Computer Vision Systems*, vol. 7963 of *Lecture Notes in Computer Science*, pp. 31–41. Springer, 2013.

[23] A. Bhandari, A. Kadambi, R. Whyte, C. Barsi, M. Feigin, A. Dorrington, and R. Raskar, "Resolving multipath interference in time-of-flight imaging via modulation frequency diversity and sparse regularization," *Opt. Lett.*, vol. 39, no. 6, pp. 1705–1708, 2014.

[24] M. Nilsson, "Estimation of tree heights and stand volume using an airborne lidar system," *Remote Sensing of Environment*, vol. 56, no. 1, pp. 1–7, 1996.